

# Rethinking Few-Shot Image Fusion: Granular Ball Priors Enable General-Purpose Deep Fusion

Minjie Deng, Yan Wei, Hao Zhai\*, An Wu, Yuncan Ouyang, Qian Yao Peng

**Abstract**—In image fusion tasks, the absence of real fused images as priors presents a fundamental challenge. Most deep learning-based fusion methods rely on large-scale paired datasets to extract global weighting features from raw images, thereby generating fused outputs that approximate real fused images. In contrast to previous studies, this paper explores few-shot training of neural networks under the condition of having prior knowledge. We propose a novel fusion framework named GBFF, and a Granular Ball Significant Extraction algorithm specifically designed for the few-shot prior setting. All pixel pairs involved in the fusion process are initially modeled as a Coarse-Grained Granular Ball. At the local level, Fine-Grained Granular Balls are used to slide through the brightness space to extract Non-Salient Pixel Pairs, and perform splitting operations to obtain Salient Pixel Pairs. Pixel-wise weights are then computed to generate a pseudo-supervised image. At the global level, pixel pairs with significant contributions to the fusion process are categorized into the Positive Region, while those whose contributions cannot be accurately determined are assigned to the Boundary Region. The Granular Ball performs modality-aware adaptation based on the proportion of the positive region, thereby adjusting the neural network's loss function and enabling it to complement the information of the boundary region. Extensive experiments demonstrate the effectiveness of both the proposed algorithm and the underlying theory. Compared with state-of-the-art (SOTA) methods, our approach shows strong competitiveness in terms of both fusion time and image expressiveness. Our code is publicly available at:

**Index Terms**—Granular Ball, Image fusion, Few-shot, Deep learning

## I. INTRODUCTION

**D**UE to the inherent limitations of individual sensors, images captured by a single sensor often fail to comprehensively represent all information within the field of view [1]. The goal of image fusion is to integrate complementary information from multiple sensors, merging images of different modalities to produce a more informative and comprehensive representation. For instance, visible light images captured at night cannot reveal thermal sources in dark regions, whereas infrared imaging can effectively highlight such thermal information [2]. By leveraging the strengths of various imaging modalities, fused images offer enhanced content and quality, making them highly valuable in applications such as medical imaging, surveillance, target recognition, and image segmentation [3].

In past research, significant progress has been made in various image fusion domains, including multi-focus image fusion, multi-exposure image fusion, infrared and visible light image fusion, and medical image fusion. Existing fusion methods can be broadly categorized into traditional approaches and deep learning-based approaches. Traditional methods typically

rely on image decomposition techniques to extract features at different scales and in different domains for fusion [4]. However, as the demand for practical, real-world applications grows, these algorithmic designs have become increasingly complex and less adaptable. As a result, deep learning-based methods have gradually become mainstream. These approaches can be further divided into CNN-based, GAN-based, Transformer-based, and hybrid methods that integrate traditional techniques. Although these methods have demonstrated impressive performance, a key limitation remains: the lack of real fused images as ground truth in cross-modality fusion tasks. Consequently, most methods rely on large-scale datasets and require multiple iterations to generate results that approximate real fused images, which is often time-consuming. This presents practical challenges, such as long deployment periods and delayed model updates, in real-world applications.

To address the aforementioned challenges, we introduce Granular Balls into the domain of image fusion and design a granular saliency extraction algorithm with both global and local perception. This algorithm provides priors for the structural information and weight assignment during the neural network training, thus enabling few-shot learning for image fusion. Previous studies have shown that in most cases, pixel pairs with similar luminance across source images tend to carry redundant or overlapping information, while those with significant luminance differences are more likely to contain complementary information and exhibit salient behavior in the fusion process.[5], [6] Based on this prior, we operate in the luminance space, where pixel pairs with similar brightness are considered less contributive to fusion. At the local level, we employ fine-grained adaptive granular balls to extract pixel pairs with non-salient behavior and compute their weights based on the scale of granular ball boundaries.

This results in a pixel-level weight map used to generate a pseudo-supervised image. At the global level, salient pixel pairs are defined as the positive region, while pixel pairs lacking prior saliency are categorized as the boundary domain, whose ultimate behavior is determined by the neural network. The proportion of positive region pixels reflects the confidence of the pseudo-supervised image and serves as a prior for setting the loss function weight. Additionally, granular balls perceive modality-specific characteristics of the fused image through positive region, enabling targeted weight adjustment. Together, the pseudo-supervised image and the adaptive weight setting jointly guide the network toward rapid convergence. In summary, our contributions are as follows:

- We propose an adaptive Granular Ball-based saliency ex-

traction algorithm for general image fusion. This method enables not only the local extraction of salient pixel pairs and computation of their fusion weights, but also the global perception of modality characteristics, providing an effective prior for adaptive fusion under diverse scenarios.

- To the best of our knowledge, this work is the first to achieve few-shot training for a general image fusion model across multiple modalities. By introducing adaptive Granular Balls as prior guidance, the proposed framework successfully performs fast and effective fusion with only 10 training image pairs per modality, establishing a novel paradigm for few-shot learning in the image fusion domain.
- A complementary learning framework is established between Granular Balls and neural networks, where priors guide salient region learning while the network compensates for uncertain regions, resulting in fast convergence and high-quality fusion within 100 training epochs.
- Compared with existing methods, the proposed approach achieves faster and more efficient image fusion. Extensive experiments demonstrate the effectiveness and rationality of the algorithm. Quantitative and qualitative results on public datasets show that our method attains competitive performance against several state-of-the-art (SOTA) techniques.

The remainder of this paper is organized as follows. Section II provides a brief overview of representative image fusion techniques and introduces the fundamentals of granular computing. Section III presents the proposed framework in detail, including its structural design and algorithmic implementation. Section IV compares our method with several state-of-the-art approaches, offering both qualitative and quantitative analysis. Section V conducts additional experimental evaluations, including ablation studies to validate the contribution of each component. Section VI concludes the paper and discusses potential future directions.

## II. RELATED WORK

In this section, we will introduce the methods and developments of image fusion, as well as the theory and applications of granular computing.

### A. Image Fusion

Image fusion requires methods that can extract features from different modality images and highlight the effective information from each modality after fusion, thereby fully representing the real scene [7]. In past research, researchers primarily used methods such as multi-scale transformations, subspace analysis, and sparse representation. As the application scenarios became increasingly complex, some researchers began to combine these methods to enhance information extraction capabilities[8]. Early researchers used Laplacian pyramids (LP) to decompose images across different frequency bands, and later utilized dual-tree complex wavelet transform (DWCWT) to extract effective information through different filtering for image fusion. However, wavelets have poor edge

extraction capabilities, leading researchers to propose the curvelet transform method, which effectively captures edge information. To enhance the representation of structural information in fusion, guided filtering (GFF) [9] was also applied to image fusion. Additionally, Liu et al. combined sparse matrix representation with traditional transformation methods to achieve good results in extracting effective information from fused images[10].

However, in real-world applications, image processing algorithms often suffer from poor generalizability as usage demands increase. This leads to increasingly complex designs, posing significant challenges for practical deployment [8]. With the rise of deep learning, Li et al. were the first to introduce it into image fusion [11], making it a mainstream approach in the field. Encoder-decoder networks, such as DeepFuse [12], demonstrated strong detail extraction capabilities in infrared and visible light fusion. Building upon this, IFCNN [13] utilized pre-trained networks for general-purpose fusion, while U2Fusion [14] designed a loss function that implicitly guides cross-modality fusion using saliency weights. In contrast to CNNs, Generative Adversarial Networks (GANs) use a discriminator to evaluate the generated results. FusionGAN [15] first introduced GANs to image fusion, and Ma et al. further proposed DDCGAN [16] by incorporating multiple discriminators to improve accuracy. Transformers, known for their long-range dependency modeling [17], were applied to image fusion by Ma et al. through SwinFusion [18], which treats image patches as tokens. Hybrid approaches combining traditional methods with deep learning have also emerged. For instance, MMIF-INET integrates wavelet decomposition with invertible neural networks for medical image fusion [19]. Moreover, MetaFusion [20] uses meta-feature interaction for IR-VIS fusion. ZMFF [21], [22] introduces deep priors for sample-free multi-focus fusion. Despite these advances, many deep models—especially those based on CNNs and Transformers—require large-scale datasets to train effectively [23], [24]. Despite the promising results achieved by deep learning-based methods, practical deployment remains challenging. Approaches based on CNNs and Transformers typically require large-scale datasets to train models and extract parameters from source images. Meanwhile, sample-free methods such as ZMFF are computationally expensive, with each fused image requiring considerable processing time. Moreover, deep learning methods that rely on traditional priors struggle to determine an adaptive fusion scale. These limitations collectively hinder the rapid deployment and few-shot application of image fusion techniques.

### B. Granular Ball Computing

Rough sets are widely used to model uncertainty in data, while ball granules offer a granulation-based approach to simplify fine-grained data, typically represented by a centroid and a radius within a spatial Granular Ball model [25], [26]. Building upon these foundations, researchers proposed the GBNRS method, which integrates granulation with approximation theory to handle continuous data more effectively [27]. Subsequently, Granular Ball clusters were introduced into

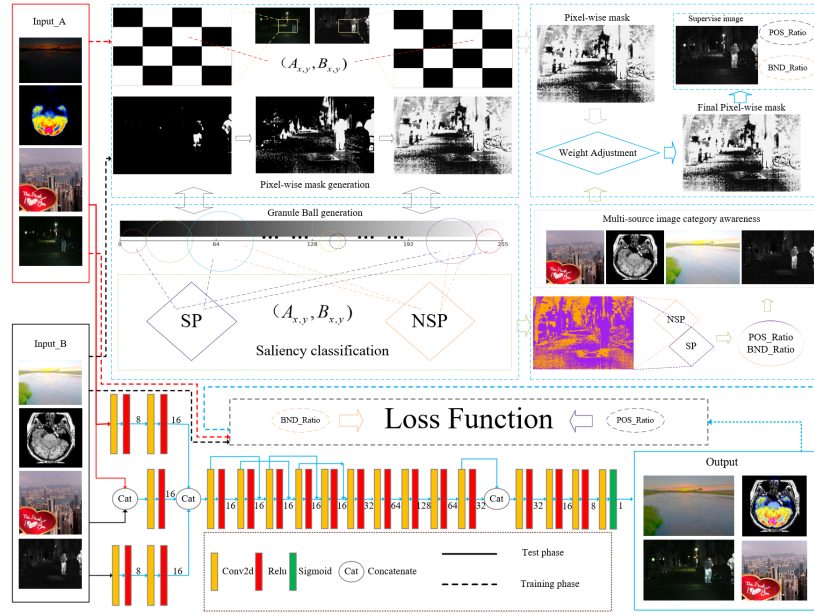


Fig. 1. The overall framework of GBFF, where the dashed parts in the diagram are algorithms and modules used only during the training phase, and the solid parts are those needed in both the testing and training phases.

clustering tasks to model instance relationships, leading to the Ball k-means algorithm, which significantly reduces spatial complexity during clustering [28]. Granular Ball computing has demonstrated strong potential in data analysis and uncertainty modeling. However, in the field of image processing, due to the lack of a unified modeling framework, existing ball granule-based methods have struggled to effectively capture relationships between image regions or modalities.

To address the above challenges, we map the original fused images into a brightness subspace and propose a Granular Ball Significant Extraction algorithm, which models pixel pairs based on their saliency in the brightness space. By integrating the Granular Ball mechanism with neural networks, we provide both structural priors and weight guidance, forming a complementary relationship between the Granular Ball and the network. This synergy enables few-shot training for general-purpose image fusion. The following sections will detail the overall structure and algorithmic implementation of the proposed method.

### III. PROPOSED METHODS

In this section, we will introduce the overall framework process according to the training phase and the testing phase, and then provide a detailed explanation of the principles of the Granular Ball swarm algorithm, the network structure, and the configuration of the loss function.

#### A. Framework

As shown in the Fig.1, the structural diagram of our framework is fully presented, including the settings of each module in the network. It is important to note that the dashed parts of the structural diagram are modules used only during the training phase, while the solid parts are used in both the testing and training phases. Here, SP refers to significant pixel

pairs, and NSP refers to non-significant pixel pairs. We have two input paths, A and B, which can be interchanged freely. All input images will be converted to the YCbCr color space. In the network structure section, the numbers on the input paths and output paths represent the number of feature map channels, and all convolution modules in the network use 3x3 convolution kernels.

#### B. Granular Ball generation

The brightness space of the original fused image carries the majority of the informative content, where the luminance of each pixel is responsible for representing image information. Since pixels appear in pairs during the fusion process, we construct fine-grained Granular Balls in the brightness space to serve as local-scale representations.

**Definition 1.** We define a granular ball  $\mathcal{G}(\mu, r)$  in the brightness space as:

$$\mathcal{G}(\mu, r) = \{x \in \mathbb{R} \mid |x - \mu| \leq r\}, \quad \mathcal{G}(\mu, r) \subseteq [0, 255] \quad (1)$$

Given a pair of source images  $A$  and  $B$ , a pixel at position  $(x, y)$  falls within the granular ball if:

$$\begin{aligned} (x, y) &\in \mathcal{P}(\mu, r) \\ \text{s.t. } A_{x,y} &\in \mathcal{G}(\mu, r) \vee B_{x,y} \in \mathcal{G}(\mu, r) \end{aligned} \quad (2)$$

#### C. Granular Ball Significant Extraction

At the fine-grained level, in order to characterize the information difference between pixel pairs in the brightness space, we define the pixel pairs within each Granular Ball accordingly.

**Definition 2.** Each pixel pair  $(A_{x,y}, B_{x,y})$  from the source images is categorized into :

**NSP:** Both pixels fall within the granular ball.

$$\begin{aligned} & (A_{x,y}, B_{x,y}) \in \mathcal{NSP} \\ \text{s.t. } & A_{x,y} \in \mathcal{G}(\mu, r) \wedge B_{x,y} \in \mathcal{G}(\mu, r) \end{aligned} \quad (3)$$

**SP:** Only one of the pixels lies within the granular ball.

$$\begin{aligned} & (A_{x,y}, B_{x,y}) \in \mathcal{SP} \\ \text{s.t. } & A_{x,y} \in \mathcal{G}(\mu, r) \wedge B_{x,y} \notin \mathcal{G}(\mu, r) \\ & \vee A_{x,y} \notin \mathcal{G}(\mu, r) \wedge B_{x,y} \in \mathcal{G}(\mu, r) \end{aligned} \quad (4)$$

During the sliding process of fine-grained Granular Balls, there is insufficient prior knowledge to directly infer salient pixel pairs. As a result, the algorithm tends to first extract non-salient pixel pairs with similar brightness values. Meanwhile, we define the purity of each Granular Ball to describe its local state during the extraction process. Additionally, we introduce the concepts of the positive domain and the boundary domain to represent global information at a coarse-grained level.

**Definition 3.** Given a granular ball  $\mathcal{G}(\mu, r)$ , we define the purity of the granular ball as the proportion of non-salient pairs (NSP) within it:

$$\text{Purity}(\mathcal{G}) = \frac{|\mathcal{NSP}|}{|\mathcal{NSP}| + |\mathcal{SP}|} \quad (5)$$

where,  $|\mathcal{NSP}|$  and  $|\mathcal{SP}|$  denote the number of pixel pairs classified as non-salient and salient, respectively, under the current granular ball  $\mathcal{G}(\mu, r)$ .

**Definition 4.** The pixel pairs in images are interpreted as follows:

- The set of **salient pairs** (SP) corresponds to the **positive region**:

$$\mathcal{POS}(A, B) = \{(x, y) \mid (A_{x,y}, B_{x,y}) \in \mathcal{SP}\} \quad (6)$$

- The set of **non-salient pairs** (NSP) corresponds to the **boundary region**:

$$\mathcal{BND}(A, B) = \{(x, y) \mid (A_{x,y}, B_{x,y}) \in \mathcal{NSP}\} \quad (7)$$

#### D. Granular Ball Significant Extraction

As illustrated in the Fig.2,  $\mathcal{NSP}$  (non-salient pixel pairs) are extracted locally through the sliding of coarse Granular Balls, while  $\mathcal{SP}$  (salient pixel pairs) are extracted during the splitting process. For non-salient pairs, a greedy strategy is adopted to estimate their weights roughly, whereas salient pixel pairs aim to capture as much informative content as possible. By combining the sliding and splitting of fine-grained Granular Balls, all pixel pairs can be classified and assigned weights. The complete process of pixel pair extraction and weight computation is detailed in Algorithm 1.

---

#### Algorithm 1: Granular Ball Significant Extraction

---

**Require:** Input images  $A, B$

**Require:** Granular ball radius  $r$ , initial mask  $X = 0$ , initial ranges  $E_1, E_2$

**Ensure:** Final fusion mask  $X, \mathcal{SP}, \mathcal{NSP}$

```

1: /* Function AssignSP( $E_{\text{low}}, E_{\text{high}}$ ) */
2: for all  $(x, y) \in \mathcal{SP}$  and  $X_{x,y} = 0$  do
3:   if  $A_{x,y}, B_{x,y} \in [E_{\text{low}}, E_{\text{high}}]$  then

```

```

4:     if  $A_{x,y} > B_{x,y}$  then
5:        $X_{x,y} = 0.95$ 
6:     else
7:        $X_{x,y} = 0.05$ 
8:     end if
9:   end if
10: end for
11: /* Function AssignNSP( $E_{\text{low}}, E_{\text{high}}$ ) */
12: for all  $(x, y) \in \mathcal{NSP}$  and  $X_{x,y} = 0$  do
13:   if  $A_{x,y}, B_{x,y} \in [E_{\text{low}}, E_{\text{high}}]$  then
14:      $D_1 = |\max(A_{x,y}, B_{x,y}) - E_{\text{high}}|$ 
15:      $D_2 = |\max(A_{x,y}, B_{x,y}) - E_{\text{low}}|$ 
16:      $\omega = \max(D_1, D_2) / ((E_{\text{high}} - E_{\text{low}}) + 10^{-6})$ 
17:      $\omega = \min(\omega, 0.95)$ 
18:     if  $A_{x,y} \geq B_{x,y}$  then
19:        $X_{x,y} = \max(\omega, 0.05)$ 
20:     else
21:        $X_{x,y} = 1 - \max(\omega, 0.05)$ 
22:     end if
23:   end if
24: end for
25: /* Main Procedure */
26: Initialize  $\mathcal{SP} = \emptyset, \mathcal{NSP} = \emptyset$ 
27:  $E_1 = 255, E_2 = E_1 - 2r$ 
28: while there exist unassigned pixels in  $X$  do
29:   if  $(E_1 - E_2) > 6 \cdot r$  then
30:     step =  $\lfloor (E_1 - E_2) / 2 \rfloor$ 
31:     rangeLow =  $E_1 - \text{step}$ , rangeHigh =  $E_1$ 
32:     Call AssignSP(rangeLow, rangeHigh)
33:      $E_1 = \text{rangeLow}$ 
34:   end if
35:   while  $E_1 > E_2$  and no unprocessed pixel in  $[E_2, E_1]$  do
36:      $E_1 = E_1 - 1$ 
37:     if  $E_1 \leq E_2$  then
38:        $E_2 = \max(E_2 - 2r, 0)$ 
39:        $E_1 = E_2$ 
40:     end if
41:   end while
42:   Call AssignSP( $E_2, E_1$ )
43:   Call AssignNSP( $E_2, E_1$ )
44:    $E_2 = \max(E_2 - 2r, 0)$ 
45:    $\mathcal{SP}', \mathcal{NSP}' = \{\text{newly unprocessed pixels in } [E_2, E_1]\}$ 
46:   Purity =  $\frac{|\mathcal{NSP}'|}{|\mathcal{SP}'| + |\mathcal{NSP}'|}$ 
47:   if Purity = 1 or  $E_2 < \delta$  then
48:     break
49:   end if
50: end while
51: return  $X, \mathcal{SP}, \mathcal{NSP}$ 

```

---

The second part of the algorithm performs modality perception, as illustrated in Algorithm 2. The Granular Ball Significant Extraction yields global  $\mathcal{NSP}$  (non-salient pixel pairs) and  $\mathcal{SP}$  (salient pixel pairs), which are used to determine the ratio between the positive domain and the boundary domain. This positive domain ratio serves as a cue for modality percep-



tion, enabling adaptive weight adjustment. The  $r_{POS}$  will be further explained in the experimental section. In this paper, modality perception is primarily applied to multi-exposure image fusion. Finally, the pseudo-supervised image and loss function weight guidance for the neural network are obtained through this process.

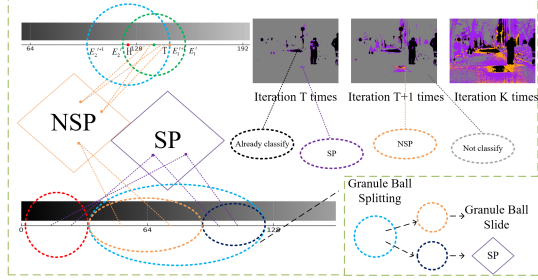


Fig. 2. The process illustrates how non-salient pixel pairs are extracted through the sliding of Granular Balls, while salient pixel pairs are identified during the splitting phase, highlighting the dynamic changes in pixel pair classification throughout the extraction procedure.

---

#### Algorithm 2: Modal Perception

---

**Require:** Final mask  $X$ , Classification  $NSP$ ,  $SP$ , Input images  $A, B$

**Ensure:** Supervise image  $Y$ , Output  $r_{BND}, r_{POS}$

- 1: Count total number of pixels  $N$  in  $X$
  - 2: Compute  $POS$  ratio:  $r_{POS} = \frac{N_{SP}}{N}$
  - 3:  $r_{BND} = 1 - r_{POS}$
  - 4: **if**  $r_{POS} > 0.95$  **then**
  - 5:   Identify all  $(x, y)$  from  $POS$
  - 6:   **for all** such pixels  $(x, y)$  **do**
  - 7:      $X_{x,y} = 0.5$
  - 8:      $r_{BND}, r_{POS} = 0.5, 0.5$
  - 9:   **end for**
  - 10: **end if**
  - 11:  $Supervise = X * A + (1 - X) * B$
  - 12: **return**  $Y, r_{BND}, r_{POS}$
- 

#### E. Multi-source input fusion strategy

The neural network trained by our method has the ability to respond to salient information and edges, as shown in Fig.3. By sequentially inputting multi-source images into the fully trained neural network, the network can extract salient information, thereby generating an image fused with salient information at each fusion step, ultimately resulting in a fused image that contains information from multiple source images.

#### F. Loss Function

Through the Granular Ball Significant Extraction algorithm, we obtain a pseudo-supervised image that provides structural priors, as well as  $r_{POS}$  and  $r_{BND}$ , which are used to guide the configuration of the loss function. The loss function is designed based on these components. We define the ideal fused image as comprising three key types of information: (1) the spatial structural information derived from the pseudo-supervised image, (2) the boundary information, where POS

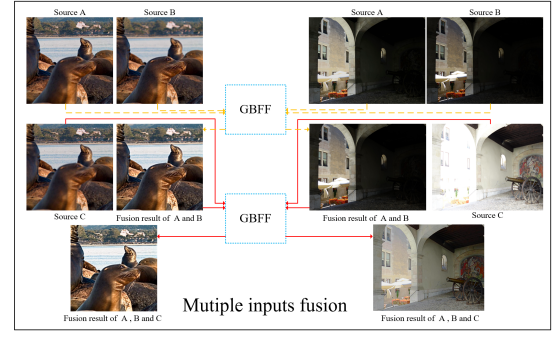


Fig. 3. Multiple inputs fusion process

determines salient boundary features and BND preserves uncertain boundary cues from the original images, and (3) the high-frequency details contained in the original fused image. Accordingly, the total loss is divided into three components:

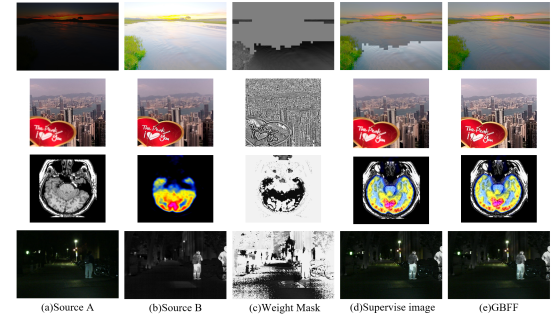


Fig. 4. To better visualize the significance extraction process of Granular Balls during image weight computation, the image is divided into small patches of size 128×128. In subfigure (c) Weight Mask, the gray areas indicate regions whose weights have been adaptively adjusted. Subfigure (d) Supervise Image shows the pseudo-supervised image generated based on the weight mask.

#### a) Structural Similarity Loss:

$$\mathcal{L}_{ssim} = 1 - \text{SSIM}(O, S) \quad (8)$$

$$\text{SSIM}(O, S) = \frac{(2\mu_O\mu_S + C_1)(2\sigma_{OS} + C_2)}{(\mu_O^2 + \mu_S^2 + C_1)(\sigma_O^2 + \sigma_S^2 + C_2)} \quad (9)$$

where  $\mu_O, \mu_S$  are local means,  $\sigma_O^2, \sigma_S^2$  are variances, and  $\sigma_{OS}$  is the covariance. Constants  $C_1$  and  $C_2$  stabilize the division.

#### b) Sobel Gradient Loss:

To guide the fusion process with edge-aware gradient information, we use the Sobel operator to extract gradients:

$$G_x = \begin{bmatrix} -1 & 0 & +1 \\ -2 & 0 & +2 \\ -1 & 0 & +1 \end{bmatrix}, \quad G_y = \begin{bmatrix} -1 & -2 & -1 \\ 0 & 0 & 0 \\ +1 & +2 & +1 \end{bmatrix} \quad (10)$$

The gradient magnitude is computed as:

$$\text{Sobel}(I) = \sqrt{G_x^2 + G_y^2} \quad (11)$$

Since the confidence of the pseudo-supervised image is determined by the proportion of the positive region, denoted as  $r_{POS}$ , the boundary loss function is defined as:

$$G_{\text{target}} = r_{POS} \cdot \text{Sobel}(S) + r_{BND} \cdot (\text{Sobel}(A) + \text{Sobel}(B)) \quad (12)$$

where the  $A$  and  $B$  are original fused images. The Sobel loss minimizes the L1 difference between the output gradient and this guided target. The second part of loss function is:

$$\mathcal{L}_{\text{Sobel}} = \|\text{Sobel}(O) - \text{Sobel}(G_{\text{target}})\|_1 \quad (13)$$

#### c) Laplacian Loss:

The Laplacian filter is applied to all input and target images to extract high-frequency energy information:

$$\Delta = \begin{bmatrix} 0 & 1 & 0 \\ 1 & -4 & 1 \\ 0 & 1 & 0 \end{bmatrix} \quad (14)$$

Therefore, the third part of the loss function is:

$$\mathcal{L}_{\text{Lap}} = \|\Delta T - \Delta X\|_1 + \|\Delta T - \Delta Y\|_1 \quad (15)$$

Finally, we obtain the loss function for the entire network:

$$\mathcal{L}_{\text{total}} = \mathcal{L}_{\text{ssim}} + \mathcal{L}_{\text{Lap}} + \mathcal{L}_{\text{Sobel}} \quad (16)$$

## IV. EXPERIMENTAL RESULTS AND ANALYSIS

### A. Experimental Setup

For the task of fusing infrared and visible light images (VIF), we selected 5 pairs of images from the MSRS[2] and TNO datasets[29] as the training set. For medical image fusion (MIF), we selected 10 pairs of images from the Harvard (PET-MRI) dataset[30] as the training set. For multi-exposure image fusion (MEF), we selected 10 pairs of images from the MEFB dataset[31] as the training set. Finally, for the multi-focus image fusion task (MFF), we selected 10 pairs of images from the Lytro dataset[32] as the training set. In the subsequent steps, we will use the images from the datasets that were not used in training as the test set. To validate generalizability, we will add the RoadScene dataset as a test set for the infrared and visible light image fusion task, and the MFI-WHU dataset[33] as a test set for multi-focus fusion.

During the training phase, to improve the robustness of the neural network, all input images are cropped to a size of 128×128 with a stride of 64 and a batch size of 16. To augment the dataset, we apply random flipping and shuffling within each batch. The total number of training epochs is set to 100. All experiments are conducted on a system equipped with an RTX 3090 GPU and an Intel i5-13600KF CPU.

### B. Multimodal image fusion

In this section, we will compare our method with the following state-of-the-art (SOTA) methods for general image fusion: (c) DDBFusion[34], (d) DeFusion[35], (e) IFCNN, (f) SDNET[11], (g) SwinFusion, and (h) U2Fusion. To demonstrate the effectiveness of our method, we will introduce a dedicated SOTA method for each type of modality image fusion, specifically: (i) MetaFusion for infrared and visible light fusion, (j) MMIF-INET for MRI and PET image fusion, (k) ZMFF for multi-focus image fusion, and (l) SAMT-MEF[36] for multi-exposure image fusion.

In the quantitative analysis section, we will use the following evaluation metrics: MI (to assess the amount of information contained in the fused image), SD (to measure the contrast of the fused image), PSNR (to evaluate the reconstruction quality of the fused image), VIF (to assess the visual fidelity of the fused image), Qab (to evaluate the structural preservation of the fused image), EN (to assess the information entropy of the fused image), SF (to evaluate the spatial frequency of the fused image), and AG (to assess the clarity of the fused image). The higher the values of these evaluation metrics, the better the quality of the fused image. For ease of observation, we will use bold black to mark the optimal indicators and underline the sub-optimal indicators.

1) *Infrared and visible image fusion:* As shown in Fig.5, compared to the methods being compared, our method demonstrates a stronger advantage in the detail texture of visible light images and infrared features, resulting in fused images with less noise and more distinct boundaries. For quantitative analysis, we used MI, SD, PSNR, VIF, and Qab. The comparison results with various methods are shown in Table I. Our method shows a strong advantage in the amount of information, fidelity, and structural retention of the fused image, and it also achieved second place in other evaluation metrics. Overall, the fused images produced by our method demonstrate a more competitive performance, capable of completing fusion tasks with fewer samples, showcasing good generalization ability.

2) *Medical image fusion:* The comparison results are shown in Fig.6. The fused images obtained from GBFF demonstrate a stronger advantage in texture details and edge performance, preserving the features of the PET images while also showcasing the texture characteristics of the MRI images. As shown in Table II, the GBFF method exhibits optimal results in the quantitative analysis of EN, MI, and PSNR values, indicating an advantage in the information content and contrast of the fused images. Additionally, the suboptimal SD

TABLE I  
QUANTITATIVE COMPARISON OF VARIOUS MEDICAL IMAGE FUSION METHODS IS CONDUCTED ON THE MSRS, ROADSCENE, AND TNO DATASETS.

Method	MSRS					RoadScene					TNO				
	MI	SD	PSNR	VIF	Qab	MI	SD	PSNR	VIF	Qab	MI	SD	PSNR	VIF	Qab
BDBFusion	2.210	28.435	19.745	0.342	0.380	2.681	44.405	14.508	0.254	0.370	2.497	44.377	15.475	0.224	0.265
DeFusion	<u>3.092</u>	34.908	22.363	0.489	0.505	3.110	35.274	16.975	0.228	0.372	<u>2.746</u>	30.508	14.581	0.238	0.348
IFCNN	2.836	35.331	<b>22.900</b>	<u>0.502</u>	<u>0.583</u>	3.000	38.350	<u>16.987</u>	0.252	<u>0.407</u>	2.505	33.188	15.561	0.326	<u>0.471</u>
SDNET	0.570	27.364	12.118	0.019	0.026	0.988	36.904	12.451	0.026	0.034	2.661	26.462	11.163	0.023	0.046
SwinFusion	2.262	26.058	17.311	0.303	0.284	<u>3.190</u>	43.828	15.837	0.257	0.374	2.492	39.243	14.908	0.268	0.469
U2Fusion	2.262	26.058	17.311	0.303	0.284	3.025	39.830	14.945	0.195	0.390	2.110	28.594	15.665	0.281	0.337
MetaFusion	1.799	<b>39.189</b>	21.481	0.530	0.488	2.240	<b>51.148</b>	15.539	<u>0.274</u>	0.347	1.844	<u>40.321</u>	<b>16.513</b>	<b>0.423</b>	0.352
GBFF	<b>3.306</b>	<u>38.499</u>	<u>22.388</u>	<b>0.533</b>	<b>0.591</b>	<b>3.351</b>	<u>46.254</u>	<b>17.333</b>	<b>0.324</b>	<b>0.425</b>	<b>2.892</b>	<b>41.378</b>	<u>15.566</u>	<u>0.354</u>	<b>0.475</b>

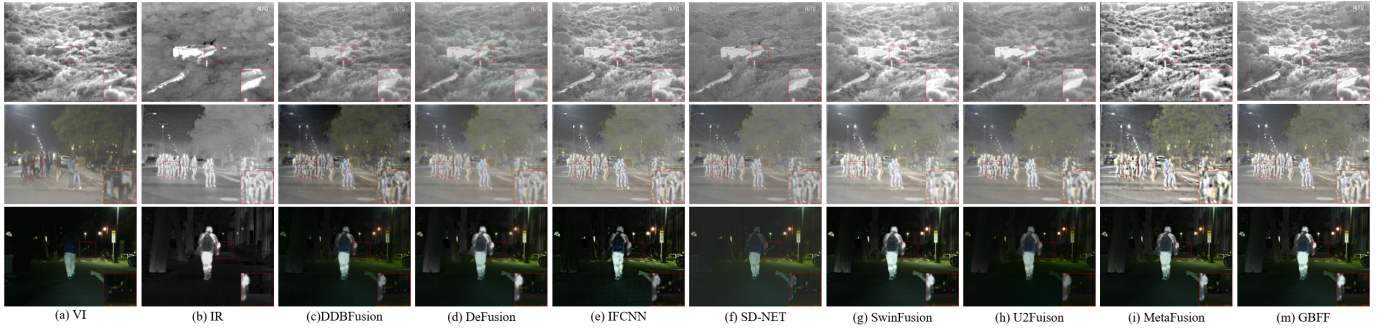


Fig. 5. Select the fusion results of 3 typical images from TNO, RoadScene, and MSRS datasets for qualitative comparison.

and Qab values also indicate that the fused images obtained by the GBFF method are correlated with the original fused images.

TABLE II

QUANTITATIVE COMPARISON OF VARIOUS MEDICAL IMAGE FUSION METHODS IS CONDUCTED ON THE HARVARD (PET-MRI) DATASET.

Harvard (PET-MRI) Method	Metrics				
	EN	MI	SD	PSNR	Qab
BBDFFusion	5.209	3.018	78.647	16.691	0.475
DeFusion	5.183	2.922	77.806	19.374	0.575
IFCNN	5.041	2.890	82.178	19.933	0.629
SDFusion	5.491	2.835	67.487	16.079	0.541
SwinFusion	5.233	2.548	83.406	18.956	0.600
U2Fusion	5.555	3.040	70.196	15.722	0.336
MMIF-INET	5.024	3.031	<b>91.864</b>	19.305	<b>0.672</b>
GBFF	<b>5.594</b>	<b>3.042</b>	<u>85.484</u>	<b>20.104</b>	<u>0.632</u>

3) *Multi-focus image fusion*: As shown in Fig.7, the GBFF method benefits from the significant extraction of granules, resulting in fused images with higher boundaries and contrast compared to other methods, leading to clearer representations. As indicated in Tables III and IV, quantitative analyses on two datasets show that the GBFF method achieves optimal values in EN, SD, and Qab for fused images, indicating that the fused images maintain high contrast and information content while preserving the original fusion image information. Additionally, in terms of SF and AG, it achieved the best and second-best results on the two datasets, respectively. Overall, the GBFF method demonstrates stronger advantages and competitiveness compared to other methods.

TABLE III

QUANTITATIVE COMPARISON OF VARIOUS MEDICAL IMAGE FUSION METHODS IS CONDUCTED ON THE LYTRO DATASET.

Lytro Method	Metrics				
	EN	SD	SF	AG	Qab
BBDFFusion	<u>7.535</u>	57.153	0.023	7.556	0.189
DeFusion	7.463	54.356	0.022	6.724	0.198
IFCNN	7.523	57.096	<u>0.036</u>	<u>11.276</u>	0.235
SDNET	7.482	55.270	0.033	10.369	<u>0.244</u>
SwinFusion	7.524	56.712	0.032	9.842	<u>0.243</u>
U2Fusion	7.460	58.390	0.023	7.073	0.207
ZMFF	7.524	56.954	0.035	11.003	0.059
GBFF	<b>7.611</b>	<b>61.989</b>	<b>0.037</b>	<b>11.526</b>	<b>0.245</b>

4) *Multi-exposure image fusion*: Compared to other fusion methods, as shown in Fig.8, the GBFF method for multi-

TABLE IV

QUANTITATIVE COMPARISON OF VARIOUS MEDICAL IMAGE FUSION METHODS IS CONDUCTED ON THE MFI-WHU DATASET.

MFI-WHU Method	Metrics				
	EN	SD	SF	AG	Qab
BBDFFusion	7.312	52.557	0.033	10.464	0.035
DeFusion	7.223	49.534	0.026	8.320	0.033
IFCNN	<u>7.326</u>	52.714	<b>0.050</b>	<b>14.896</b>	0.037
SDnet	7.288	51.255	0.045	14.744	0.038
SwinFusion	7.289	51.589	0.040	12.803	0.037
U2Fusion	7.226	53.326	0.026	8.230	0.032
ZMFF	7.295	51.994	0.045	14.780	0.035
GBFF	<b>7.419</b>	<b>58.100</b>	<u>0.046</u>	<u>14.792</u>	<b>0.039</b>

exposure image fusion focuses more on the representation of texture information, avoiding texture distortion like that caused by the IFCNN method and color distortion like that caused by the SAMT-MEF method. Additionally, in high-exposure environments, the GBFF method handles light sources more smoothly, preserving details without causing halo noise. Quantitative analysis is shown in Table V, where the GBFF method achieves optimal results in EN and Qab, indicating that the fused images obtained by the GBFF method can capture more information during fusion. The suboptimal results in MI, SD, and SF suggest that the fused images have a high amount of information and contrast.

TABLE V

QUANTITATIVE COMPARISON OF VARIOUS MEDICAL IMAGE FUSION METHODS IS CONDUCTED ON THE MEFB DATASET.

MEFB Method	Metrics				
	EN	MI	SD	SF	Qab
BBDFFusion	6.730	0.722	58.406	0.027	0.028
DeFusion	6.463	0.592	38.457	0.017	0.023
IFCNN	6.888	0.465	<u>46.404</u>	<b>0.041</b>	0.027
SDNET	6.623	0.668	40.202	0.023	0.025
SwinFusion	6.212	0.703	33.387	0.012	0.017
U2Fusion	6.739	0.744	39.674	0.013	0.022
SAMT-MEF	<u>6.849</u>	<b>0.792</b>	43.505	0.024	<b>0.038</b>
GBFF	<b>6.947</b>	<u>0.678</u>	<b>46.655</b>	<u>0.028</u>	<u>0.031</u>

### C. Efficiency Analysis

In this section, we will compare the efficiency of all methods using images of size 224\*224 as a benchmark, and we will use the network's training parameters (params), floating-point operations (Flops), and the time consumed to fuse a pair



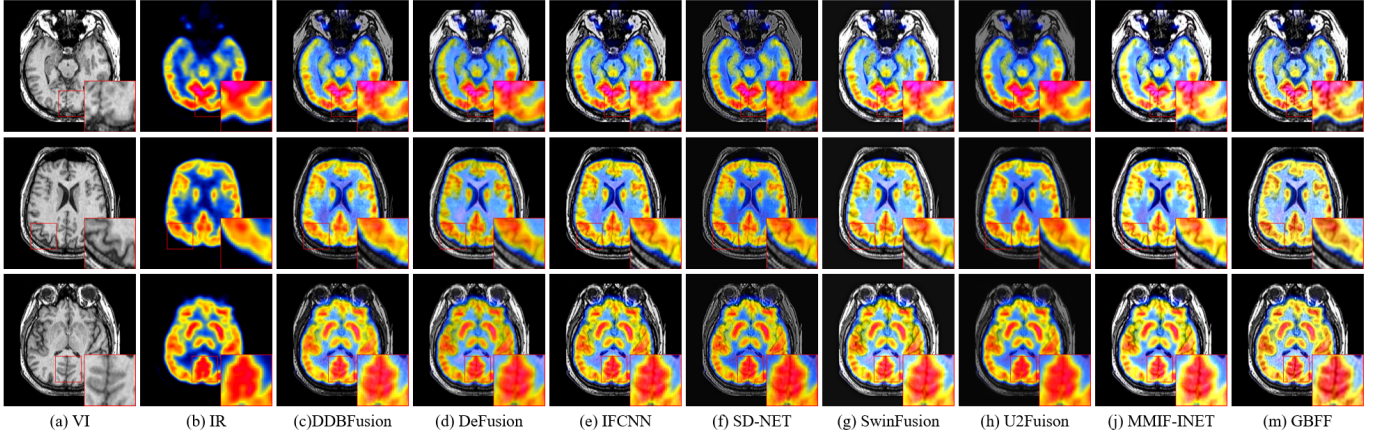


Fig. 6. Select the fusion results of 3 typical images from the Harvard (PET-MRI) dataset for qualitative comparison.



Fig. 7. Select the fusion results of 3 typical images from the MFI-WHU and Lytro datasets for qualitative comparison.



Fig. 8. Select the fusion results of 3 typical images from the MEFB dataset for qualitative comparison.

of images as metrics. As shown in Table VI, due to the fewer residual layers in the GBFF network and its simplicity, although it did not achieve the best results in terms of params, it achieved the optimal value in Flops and also performed second best in fusion time.

## V. THEORETICAL ANALYSIS AND ABLATION EXPERIMENTS

### A. Analysis of Granular Ball Significant Extraction Algorithm

In this section, we will analyze the impact of the radius of the Granular Ball on the extraction of significant pixels. Next, we will further analyze the global modal perception

mechanism of the Granular Ball, as well as the prior sources of threshold settings in the GBFF method.

#### 1) Granular Ball radius and significant pixel extraction:

The radius setting of the Granular Ball affects the maximum boundary and splitting of the Granular Ball, which in turn impacts the classification of  $SP$  and  $NSP$ , as shown in Fig.9 and Fig.10. When the radius is set too small, the sliding speed of the Granular Ball is too slow, resulting in a high number of iterations and significant computational time overhead, with  $r_{POS}$  showing no obvious changes. However, for images with multiple exposure modes, fluctuations occur

TABLE VI  
COMPARISON OF PARAMETER SIZE, COMPUTATIONAL COST, AND  
INFERENCE TIME AMONG DIFFERENT IMAGE FUSION METHODS.

Method	Params (M)	FLOPs (G)	Time (s)
BBDFFusion	3.673	184.931	0.953
DeFusion	7.874	71.551	0.426
IFCNN	<u>0.083</u>	39.932	<u>0.024</u>
SDNET	<b>0.044</b>	25.638	0.056
SwinFusion	0.973	292.537	1.467
U2Fusion	0.659	405.174	0.143
SAMT-MEF	1.176	38.450	0.174
MMIF-INET	0.749	<u>3.020</u>	0.110
ZMFF	4.670	230.380	242.790
MetaFusion	9.350	24.630	0.220
GBFF	0.261	<b>2.211</b>	<b>0.022</b>

when the Granular Ball radius is set greater than 10, which is detrimental to subsequent modal perception. Therefore, we choose a Granular Ball radius of 10, balancing iteration speed while maintaining classification effectiveness.

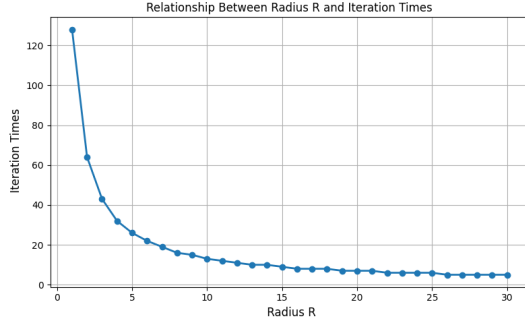


Fig. 9. The relationship between the radius of the Granular BALL and the number of iterations.

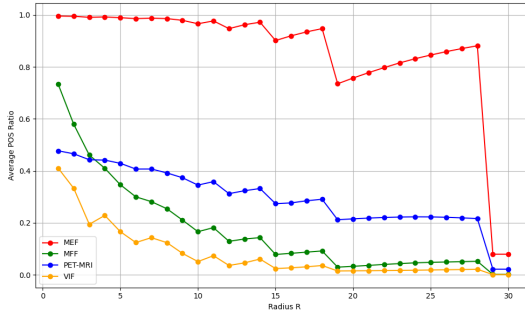


Fig. 10. The relationship between the radius and  $r_{POS}$  in the significant extraction algorithm for Granular BALL.

2) *Modal Perception*: In the method proposed in this article, a threshold of 0.95 is set as the extreme modal perception condition for  $r_{POS}$  to adjust the information ratio of multi-exposure images. As shown in Figure x, with a Granular Ball radius of 10, we statistically analyzed  $r_{POS}$  for 100 images of each modality. It can be observed that the  $r_{POS}$  obtained after Granular Ball generation classification exhibits significant clustering for images of different modalities. This allows us to set a threshold, which serves as a prior for global modal perception of the Granular Ball. Therefore, the threshold

of 0.95 we set can encompass the vast majority of multi-exposure images without affecting images of other modalities. Meanwhile, multi-exposure images that are not perceived in some multi-modal images are treated as noise images by the neural network. Previous research has confirmed that this can enhance the robustness of the neural network[37]. As shown in Table VII, after adding modal awareness, the values have all increased, indicating that the quality of the fused images has been further enhanced. From Fig.11, it can be observed that after adding modal perception, the suppression of the exposed areas has significantly improved, and the texture information is clearer.

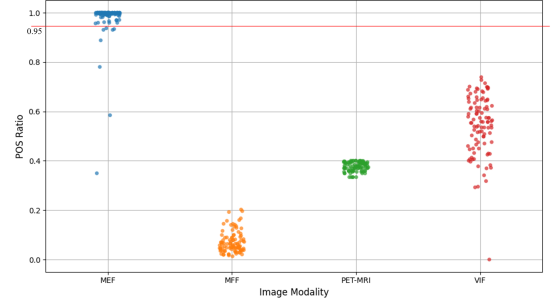


Fig. 11. In the case where the radius of the Granular BALL is 10, perform  $r_{POS}$  evaluation on 100 pairs of images with different modalities.

TABLE VII  
QUANTITATIVE COMPARISON BETWEEN W/O MODAL PERCEPTION AND GBFF.

MEFB	Metrics				
Method	EN	MI	SD	SF	Qab
w/o Modal Perception	6.654	0.548	44.550	0.015	0.022
GBFF	<b>6.947</b>	<b>0.678</b>	<b>46.655</b>	<b>0.028</b>	<b>0.031</b>

### B. Prior guided training

In this section, we conduct a comparative analysis between traditional prior-based methods and the proposed Granular Ball priors, in order to investigate the role of prior guidance in neural network training. We then perform ablation studies on two key components of the GBFF framework: weight guidance and structural guidance from the pseudo-supervised image. Finally, we explore the impact of the number of training epochs under the few-shot setting.

#### 1) Granular Ball prior and traditional method prior:

In previous studies on few-shot training, prior knowledge has been shown to effectively reduce the reliance of neural networks on large amounts of training data[38], [24], [39], [23]. Based on this observation, we incorporate prior images generated by traditional methods into our network as alternative guidance, aiming to explore how different types of priors influence the training process. Both qualitative and quantitative analyses are conducted to evaluate the impact of prior selection on fusion performance. In this section, we further introduce four traditional fusion methods to serve as priors: (c) the Curvelet fusion method based on curvelet transform, (d) the DTCWT method utilizing the dual-tree complex wavelet



TABLE VIII

QUANTITATIVE ANALYSIS IS CONDUCTED ON TRADITIONAL METHODS AND FUSION RESULTS USING TRADITIONAL METHODS AS PRIORS. FOR EACH MODALITY, THE FUSION PERFORMANCE METRICS ARE AVERAGED ACROSS ALL DATASETS.

Method	MIF					MFF					VIF					MEF				
	EN	MI	SD	PSNR	Qab	EN	SD	SF	AG	Qab	MI	SD	PSNR	VIF	Qab	EN	MI	SD	SF	Qab
Curvelet	5.496	2.023	75.933	13.019	0.348	7.431	55.412	0.038	12.461	0.065	2.185	41.972	18.041	0.407	0.490	6.891	0.162	53.707	0.018	0.009
Curvelet_prior	5.263	2.623	79.704	13.985	0.531	7.499	57.614	0.034	11.923	0.139	2.528	40.340	17.695	0.394	0.496	5.627	0.376	22.175	0.012	0.011
Dtcwt	5.455	1.988	74.314	14.629	0.333	7.429	55.450	0.038	12.513	0.061	2.537	40.647	18.265	0.395	0.490	<b>6.948</b>	0.182	<b>55.877</b>	0.018	0.009
Dtcwt_prior	5.249	2.642	82.094	14.750	0.497	7.409	52.507	0.037	11.026	0.140	2.639	41.354	18.275	0.399	0.470	6.463	0.348	18.950	0.011	0.012
GFF	5.063	3.022	78.313	12.750	0.609	7.454	55.470	0.038	12.466	0.140	2.558	38.010	17.686	0.381	0.495	6.916	0.374	45.992	<u>0.020</u>	0.021
GFF_prior	5.235	2.717	82.361	12.775	0.567	7.483	<u>58.097</u>	<u>0.040</u>	<u>12.866</u>	0.136	2.256	40.214	18.213	0.400	0.492	6.543	0.359	38.896	0.019	<u>0.024</u>
Lp	4.796	2.177	77.944	13.356	0.385	7.432	55.775	0.038	12.574	0.041	2.446	40.184	<b>18.651</b>	0.393	<u>0.496</u>	6.452	0.215	53.145	0.019	0.012
Lp_prior	5.157	2.646	77.921	14.602	0.521	7.459	55.167	0.033	11.735	<u>0.141</u>	2.682	41.422	18.205	0.391	0.481	6.343	0.360	18.811	0.012	0.012
Supervise	4.834	<b>3.231</b>	<u>85.419</u>	11.655	<u>0.619</u>	7.379	52.650	0.023	7.408	0.083	<u>3.170</u>	39.891	18.238	0.402	0.494	6.640	<u>0.639</u>	40.718	<u>0.020</u>	0.022
GBFF	<b>5.594</b>	<u>3.042</u>	<b>85.484</b>	<b>20.104</b>	<b>0.632</b>	<b>7.515</b>	<b>60.045</b>	<b>0.042</b>	<b>13.159</b>	<b>0.142</b>	<b>3.183</b>	<b>42.044</b>	<u>18.436</u>	<b>0.403</b>	<b>0.497</b>	6.947	<b>0.678</b>	46.655	<b>0.023</b>	<b>0.028</b>

TABLE IX

A QUANTITATIVE ANALYSIS IS PERFORMED ON THE FUSION RESULTS OF ABLATION EXPERIMENTS INVOLVING PRIOR GUIDANCE AND WEIGHT GUIDANCE. FOR EACH MODALITY, THE FUSION PERFORMANCE METRICS ARE AVERAGED ACROSS ALL DATASETS.

Method	MIF					MFF					VIF					MEF				
	EN	MI	SD	PSNR	Qab	EN	SD	SF	AG	Qab	MI	SD	PSNR	VIF	Qab	EN	MI	SD	SF	Qab
w/o weight	5.569	<u>3.009</u>	<u>83.072</u>	11.727	<u>0.613</u>	<u>7.384</u>	57.227	0.028	9.347	0.134	<u>3.115</u>	<u>40.586</u>	<u>17.877</u>	<b>0.417</b>	<u>0.466</u>	6.703	0.595	33.430	0.012	0.018
w/o prior	5.385	2.835	79.106	15.078	0.555	7.201	57.948	0.031	9.977	<u>0.135</u>	2.017	38.302	16.467	0.385	0.444	6.871	0.643	34.625	0.013	<u>0.024</u>
w/o prior and weight	<b>5.601</b>	2.042	59.766	7.363	0.493	7.339	55.494	0.033	11.386	0.093	1.925	33.251	8.706	0.378	0.273	6.879	0.611	42.430	0.017	0.019
GBFF	<u>5.594</u>	<b>3.042</b>	<b>85.484</b>	<b>20.104</b>	<b>0.632</b>	<b>7.515</b>	<b>60.045</b>	<b>0.042</b>	<b>13.159</b>	<b>0.142</b>	<b>3.183</b>	<b>42.044</b>	<b>18.436</b>	<u>0.403</u>	<b>0.497</b>	<b>6.947</b>	<b>0.678</b>	<b>46.655</b>	<b>0.028</b>	<b>0.031</b>

transform, (e) the GFF fusion method using guided filtering, and (h) the LP fusion method that combines Laplacian pyramid decomposition with sparse representation. Since traditional methods lack adaptive weight mechanisms, we manually set the values of  $r_{\text{POS}}$  and  $r_{\text{BND}}$  to 0.5 to balance the loss function. All other training settings, including the number of iterations and network parameters, remain consistent with those used in the GBFF method. The fusion results are illustrated in Figure 12, which compares the outputs of traditional methods and networks that use structure maps from traditional methods as priors. It can be observed that, even under few-shot conditions, networks guided by traditional priors still achieve promising results, and can partially compensate for the weaker regions present in the original traditional fusion outputs. However, compared to the GBFF method, traditional priors do not enable adaptive alignment between the network and the prior information. Although the structural priors extracted by traditional methods exhibit stronger feature representation in multi-focus and medical image fusion tasks, the final fused images produced by the GBFF-guided network outperform those obtained using traditional priors. A quantitative comparison is provided in Table VIII. Compared with standalone traditional methods, few-shot training with traditional priors achieves significant performance gains, verifying the effectiveness of the prior-guided few-shot training strategy proposed in this paper. When compared to the GBFF method, the traditional-prior variant only achieves slightly better results in the EN indicator for multi-exposure fusion, but the GBFF still consistently delivers the best performance across other metrics. This demonstrates that the design and performance of GBFF are better suited for general-purpose few-shot image fusion.

2) *Structural priors and weight-guided ablation:* In this section, we perform a step-by-step ablation of image priors and weight guidance to analyze their respective roles in few-shot neural network training. After processing with the Granular Ball, we obtain pseudo-supervised images as image priors, along with the corresponding  $r_{\text{pos}}$  and  $r_{\text{bnd}}$  values that reflect the confidence of these priors. These values are used

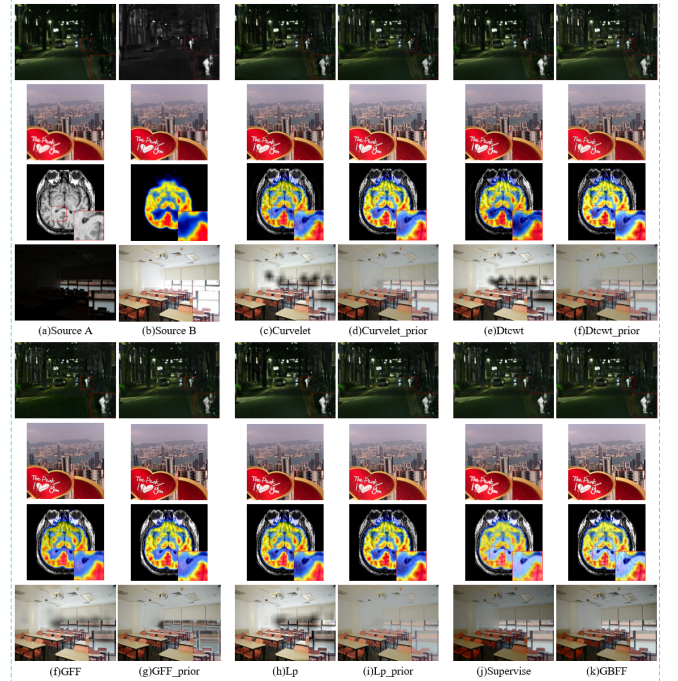


Fig. 12. Compared to traditional algorithms and few-shot methods that use fused images from traditional algorithms as priors, images (d), (f), (g), and (i) represent the fused results generated by the networks trained with the corresponding priors from (c), (e), (f), and (h), respectively. Image (j) is the fused result generated based on the Granular Ball Significant Extraction.

to guide the loss function during training. Specifically, we consider the following three settings: (c) w/o Weight: Granular Ball prior is used, but no weight guidance is provided (i.e.,  $r_{\text{POS}} = r_{\text{BND}} = 0.5$ ); (d) w/o Prior: No Granular Ball prior is used; instead, a simple 0.5-weighted fusion of the input images is used as a substitute prior; (e) w/o Prior and Weight: The network directly learns fusion without any prior or weight guidance. As shown in Figure 13, methods without prior information fail to capture salient features, while those without

TABLE X

QUANTITATIVE ANALYSIS IS CONDUCTED ON THE FUSED IMAGES OBTAINED AFTER THE ABLATION OF SPECIFIC LOSS FUNCTION COMPONENTS. FOR EACH MODALITY, THE FUSION PERFORMANCE METRICS ARE AVERAGED ACROSS ALL DATASETS.

Method	MIF					MFF					VIF					MEF				
	EN	MI	SD	PSNR	Qab	EN	SD	SF	AG	Qab	MI	SD	PSNR	VIF	Qab	EN	MI	SD	SF	Qab
supervise	4.834	<b>3.231</b>	85.419	11.655	0.619	7.379	52.650	0.023	7.408	0.083	3.170	39.891	18.238	0.402	0.494	6.640	0.639	40.718	0.020	0.022
w/o $\mathcal{L}_{lap}$	<b>5.613</b>	3.033	84.753	11.292	0.628	7.412	59.334	0.034	10.864	0.139	<b>3.184</b>	40.977	18.340	0.402	0.489	6.618	0.569	42.821	0.021	0.027
w/o $\mathcal{L}_{sobel}$	5.473	3.042	83.677	11.924	0.611	7.383	52.783	0.026	7.136	0.073	3.136	40.060	18.159	0.391	0.469	<u>6.677</u>	<u>0.646</u>	39.002	0.018	0.025
w/o $\mathcal{L}_{lap}$ and $\mathcal{L}_{sobel}$	5.506	3.053	84.060	11.538	0.604	7.370	52.046	0.024	7.127	0.087	3.162	39.654	18.195	0.399	0.464	6.433	0.488	39.210	0.020	0.025
GBFF	<u>5.594</u>	<u>3.042</u>	<b>85.484</b>	<b>20.104</b>	<b>0.632</b>	<b>7.515</b>	<b>60.045</b>	<b>0.042</b>	<b>13.159</b>	<b>0.142</b>	<u>3.183</u>	<b>42.044</b>	<b>18.436</b>	<b>0.403</b>	<b>0.497</b>	<b>6.947</b>	<b>0.678</b>	<b>46.655</b>	<b>0.028</b>	<b>0.031</b>

adaptive weight fusion struggle to preserve edge information. The fused results obtained without both priors and weights exhibit severe structural distortion, making it difficult for the network to fit the expected fused image. From Table IX, we observe that the full GBFF method achieves the best results across most evaluation metrics. This demonstrates that the combination of structural priors and weight guidance leads to the most effective fusion results.

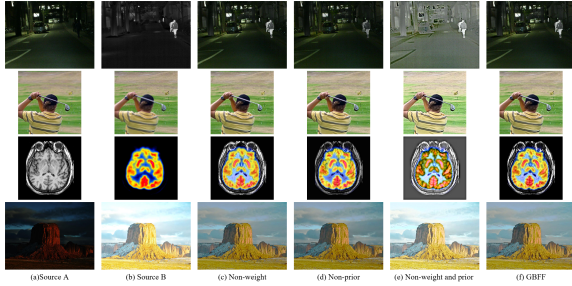


Fig. 13. The fused image obtained from the structural prior provided by the ablation supervision image and the weight adjustment, as well as the fused image obtained from training the network without using prior and weight adjustment.

3) *Selection of Train Epoch*: In Few-shot learning, due to the use of supervised images as a prior for spatial structure, and since supervised images do not possess the expressiveness of real fused images, excessive iterations of the neural network can lead to overfitting. Early stopping of iterations is beneficial for maintaining higher expressiveness in the neural network. We evaluate the relationship between the fused images and the number of iterations by measuring the average values of PSNR, EN, MI, and SD of the output images for each iteration, as well as the changes in the loss function. From Fig.14, it can be observed that after 100 iterations, the various metrics of the fused images tend to stabilize, and the loss function also stabilizes.

### C. Loss function ablation

In the GBFF method, the expected fused image is defined as a combination of the structural information from the pseudo-supervised image and salient information with confidence, further supplemented by the boundary information and high-frequency details from the original fused image to compensate for regions with low saliency confidence. In this section, we conduct an ablation study on the loss function to verify the rationality of its design. As confirmed in the previous section, when the network lacks structural priors from the pseudo-supervised image, it struggles to learn the correct fused image

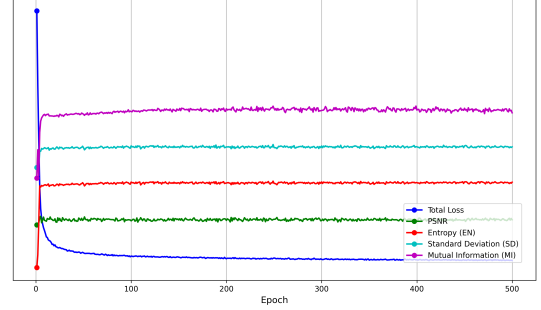


Fig. 14. As the number of iterations increases, the changes in various evaluation metrics and the loss function.

content. Therefore, we do not ablate the  $\mathcal{L}_{SSIM}$  component in this part. The experiments are divided into three settings: (a) w/o  $\mathcal{L}_{sobel}$ , (b) w/o  $\mathcal{L}_{lap}$ , and (c) w/o both  $\mathcal{L}_{sobel}$  and  $\mathcal{L}_{lap}$ . As shown in Table X, the fused images generated without boundary and detail supervision are significantly less expressive compared to those trained with the complete loss. Adding  $\mathcal{L}_{sobel}$  improves boundary sharpness, while including  $\mathcal{L}_{lap}$  enhances the network's ability to reconstruct high-frequency textures. The corresponding changes in evaluation metrics confirm the effectiveness and necessity of each component. Overall, the complete loss function setting of GBFF ensures that the fused image achieves balanced performance across all metrics, and contributes to the superior expressiveness of the fusion results.

## VI. CONCLUSION

In this paper, we proposed a general-purpose image fusion framework that leverages prior information to enable few-shot training. To address the challenge of insufficient priors for neural networks, we introduced a Granular Ball-based saliency extraction algorithm, which operates in the brightness subspace with modality-aware and adaptive saliency extraction capabilities. This algorithm provides structural priors to the network and adaptively adjusts the loss function based on the extracted information. We conducted both qualitative and quantitative comparisons with state-of-the-art (SOTA) methods and demonstrated that our approach remains effective and competitive even under few-shot conditions. Additionally, we performed experimental analyses on the radius settings of the Granular Ball and its modality perception ability. The results show that prior-guided neural networks can achieve effective fusion in few-shot scenarios, and comparisons with different prior settings validate the effectiveness of the proposed Granular Ball prior. Finally, we conducted ablation studies to



evaluate the contribution of each module and loss component in the proposed method. Although this work presents a novel paradigm for few-shot image fusion and achieves promising results across multiple representative fusion tasks, the current implementation extracts priors only from the brightness subspace, which may limit its effectiveness in more complex scenarios where information from other domains is needed. In future work, we plan to extend the Granular Ball mechanism to support joint inference across multiple subspaces, enabling more accurate and comprehensive information extraction. Furthermore, we aim to explore the use of Granular Ball priors in other few-shot tasks, such as super-resolution and image segmentation.

## REFERENCES

- [1] Y. Liu, Z. Qi, J. Cheng, and X. Chen, "Rethinking the effectiveness of objective evaluation metrics in multi-focus image fusion: A statistic-based approach," *IEEE Transactions on Pattern Analysis and Machine Intelligence*, 2024.
- [2] L. Tang, J. Yuan, H. Zhang, X. Jiang, and J. Ma, "Piafusion: A progressive infrared and visible image fusion network based on illumination aware," *Information Fusion*, vol. 83, pp. 79–92, 2022.
- [3] M. Zhou, J. Huang, K. Yan, D. Hong, X. Jia, J. Chanussot, and C. Li, "A general spatial-frequency learning framework for multimodal image fusion," *IEEE Transactions on Pattern Analysis and Machine Intelligence*, 2024.
- [4] H. Kaur, D. Koundal, and V. Kadyan, "Image fusion techniques: a survey," *Archives of computational methods in Engineering*, vol. 28, no. 7, pp. 4425–4447, 2021.
- [5] P. J. Burt and E. H. Adelson, "The laplacian pyramid as a compact image code," in *Readings in computer vision*. Elsevier, 1987, pp. 671–679.
- [6] S. Karim, G. Tong, J. Li, A. Qadir, U. Farooq, and Y. Yu, "Current advances and future perspectives of image fusion: A comprehensive review," *Information Fusion*, vol. 90, pp. 185–217, 2023.
- [7] A. P. James and B. V. Dasarathy, "Medical image fusion: A survey of the state of the art," *Information fusion*, vol. 19, pp. 4–19, 2014.
- [8] H. Zhang, H. Xu, X. Tian, J. Jiang, and J. Ma, "Image fusion meets deep learning: A survey and perspective," *Information Fusion*, vol. 76, pp. 323–336, 2021.
- [9] S. Li, X. Kang, and J. Hu, "Image fusion with guided filtering," *IEEE Transactions on Image processing*, vol. 22, no. 7, pp. 2864–2875, 2013.
- [10] Y. Liu, S. Liu, and Z. Wang, "A general framework for image fusion based on multi-scale transform and sparse representation," *Information fusion*, vol. 24, pp. 147–164, 2015.
- [11] H. Li and X.-J. Wu, "Densefuse: A fusion approach to infrared and visible images," *IEEE Transactions on Image Processing*, vol. 28, no. 5, pp. 2614–2623, 2018.
- [12] K. Ram Prabhakar, V. Sai Srikar, and R. Venkatesh Babu, "Deepfuse: A deep unsupervised approach for exposure fusion with extreme exposure image pairs," in *Proceedings of the IEEE international conference on computer vision*, 2017, pp. 4714–4722.
- [13] Y. Zhang, Y. Liu, P. Sun, H. Yan, X. Zhao, and L. Zhang, "Ifcnn: A general image fusion framework based on convolutional neural network," *Information Fusion*, vol. 54, pp. 99–118, 2020.
- [14] H. Xu, J. Ma, J. Jiang, X. Guo, and H. Ling, "U2fusion: A unified unsupervised image fusion network," *IEEE transactions on pattern analysis and machine intelligence*, vol. 44, no. 1, pp. 502–518, 2020.
- [15] J. Ma, W. Yu, P. Liang, C. Li, and J. Jiang, "Fusiongan: A generative adversarial network for infrared and visible image fusion," *Information fusion*, vol. 48, pp. 11–26, 2019.
- [16] J. Ma, H. Xu, J. Jiang, X. Mei, and X.-P. Zhang, "Ddcgan: A dual-discriminator conditional generative adversarial network for multi-resolution image fusion," *IEEE Transactions on Image Processing*, vol. 29, pp. 4980–4995, 2020.
- [17] K. Han, Y. Wang, H. Chen, X. Chen, J. Guo, Z. Liu, Y. Tang, A. Xiao, C. Xu, Y. Xu *et al.*, "A survey on vision transformer," *IEEE transactions on pattern analysis and machine intelligence*, vol. 45, no. 1, pp. 87–110, 2022.
- [18] J. Ma, L. Tang, F. Fan, J. Huang, X. Mei, and Y. Ma, "Swinfusion: Cross-domain long-range learning for general image fusion via swin transformer," *IEEE/CAA Journal of Automatica Sinica*, vol. 9, no. 7, pp. 1200–1217, 2022.
- [19] D. He, W. Li, G. Wang, Y. Huang, and S. Liu, "Mmif-net: Multimodal medical image fusion by invertible network," *Information Fusion*, vol. 114, p. 102666, 2025.
- [20] W. Zhao, S. Xie, F. Zhao, Y. He, and H. Lu, "Metafusion: Infrared and visible image fusion via meta-feature embedding from object detection," in *Proceedings of the IEEE/CVF Conference on Computer Vision and Pattern Recognition*, 2023, pp. 13 955–13 965.
- [21] X. Hu, J. Jiang, X. Liu, and J. Ma, "Zmff: Zero-shot multi-focus image fusion," *Information Fusion*, vol. 92, pp. 127–138, 2023.
- [22] T. Li, H. Wang, Z. Zhuang, and J. Sun, "Deep random projector: Accelerated deep image prior," in *Proceedings of the IEEE/CVF Conference on Computer Vision and Pattern Recognition*, 2023, pp. 18 176–18 185.
- [23] R. Zhang, J. Tan, Z. Cao, L. Xu, Y. Liu, L. Si, and F. Sun, "Part-aware correlation networks for few-shot learning," *IEEE Transactions on Multimedia*, 2024.
- [24] C. Lang, G. Cheng, B. Tu, C. Li, and J. Han, "Base and meta: A new perspective on few-shot segmentation," *IEEE Transactions on Pattern Analysis and Machine Intelligence*, vol. 45, no. 9, pp. 10669–10686, 2023.
- [25] S. Cheng, X. Su, B. Chen, H. Chen, D. Peng, and Z. Yuan, "Gbmdd: A granular-ball mean-shift outlier detector," *Pattern Recognition*, vol. 159, p. 111115, 2025.
- [26] S. Xia, C. Wang, G. Wang, X. Gao, W. Ding, J. Yu, Y. Zhai, and Z. Chen, "Gbrs: A unified granular-ball learning model of pawlak rough set and neighborhood rough set," *IEEE Transactions on Neural Networks and Learning Systems*, 2023.
- [27] S. Xia, H. Zhang, W. Li, G. Wang, E. Giem, and Z. Chen, "Gbnrs: A novel rough set algorithm for fast adaptive attribute reduction in classification," *IEEE Transactions on Knowledge and Data Engineering*, vol. 34, no. 3, pp. 1231–1242, 2020.
- [28] S. Xia, D. Peng, D. Meng, C. Zhang, G. Wang, E. Giem, W. Wei, and Z. Chen, "Ball  $k$  k-means: Fast adaptive clustering with no bounds," *IEEE transactions on pattern analysis and machine intelligence*, vol. 44, no. 1, pp. 87–99, 2020.
- [29] A. Toet, "The tno multiband image data collection," *Data in brief*, vol. 15, p. 249, 2017.
- [30] K. A. Johnson and J. A. Becker, "Whole brain atlas - mri-pet dataset," 1999, harvard Medical School, Department of Radiology. [Online]. Available: <http://www.med.harvard.edu/AANLIB/>
- [31] X. Zhang, "Benchmarking and comparing multi-exposure image fusion algorithms," *Information Fusion*, pp. 111–131, 2021.
- [32] M.-C. Tao, S. Hadap, J. Malik, and R. Ramamoorthi, "Depth estimation and specular removal for light field images," in *European Conference on Computer Vision*. Springer, 2013, pp. 628–643.
- [33] H. Zhang, Z. Le, Z. Shao, H. Xu, and J. Ma, "Mff-gan: An unsupervised generative adversarial network with adaptive and gradient joint constraints for multi-focus image fusion," *Information Fusion*, vol. 66, pp. 40–53, 2021.
- [34] Z. Zhang, H. Li, T. Xu, X.-J. Wu, and J. Kittler, "Ddbfusion: An unified image decomposition and fusion framework based on dual decomposition and bézier curves," *Information Fusion*, vol. 114, p. 102655, 2025.
- [35] P. Liang, J. Jiang, X. Liu, and J. Ma, "Fusion from decomposition: A self-supervised decomposition approach for image fusion," in *European Conference on Computer Vision*. Springer, 2022, pp. 719–735.
- [36] Q. Huang, G. Wu, Z. Jiang, W. Fan, B. Xu, and J. Liu, "Leveraging a self-adaptive mean teacher model for semi-supervised multi-exposure image fusion," *Information Fusion*, vol. 112, p. 102534, 2024.
- [37] Z. He, A. S. Rakin, and D. Fan, "Parametric noise injection: Trainable randomness to improve deep neural network robustness against adversarial attack," in *Proceedings of the IEEE/CVF conference on computer vision and pattern recognition*, 2019, pp. 588–597.
- [38] D. Ulyanov, A. Vedaldi, and V. Lempitsky, "Deep image prior," in *Proceedings of the IEEE conference on computer vision and pattern recognition*, 2018, pp. 9446–9454.
- [39] H. Xu, L. Liu, S. Zhi, S. Fu, Z. Su, M.-M. Cheng, and Y. Liu, "Enhancing information maximization with distance-aware contrastive learning for source-free cross-domain few-shot learning," *IEEE Transactions on Image Processing*, 2024.